ORIGINAL PAPER

Dynamic Fracturing Simulation of Brittle Material using the Distinct Lattice Spring Method with a Full Rate-Dependent Cohesive Law

T. Kazerani · G. F. Zhao · J. Zhao

Abstract A full rate-dependent cohesive law is implemented in the distinct lattice spring method (DLSM) to investigate the dynamic fracturing behavior of brittle materials. Both the spring ultimate deformation and spring strength are dependent on the spring deformation rate. From the simulation results, it is found that the dynamic crack propagation velocity can be well predicted by the DLSM through the implemented full rate-dependent cohesive law. Furthermore, a numerical investigation on dynamic branching is also conducted by using the DLSM code.

Keywords Dynamic fracturing · Crack propagation velocity · Rate-dependent cohesive law · DLSM

1 Introduction

A major objective in studying dynamic fracturing is to predict crack dissemination pattern and velocity. Linear elastic fracture mechanics (LEFM) theoretically suggests the Rayleigh surface wave speed v_R as the upper limit for the material crack velocity v_{cr} (Freund 1990; Broberg 1999). However, in rapid cracking of brittle solids, the crack tip zone undergoes a series of complex mechanisms such as large and nonlinear deformation, high strain rate, plasticity, micro-crack nucleation, heat diffusion, and subsequent thermal softening. These mechanisms cause the fracture energy G_f to increase when the crack velocity

increases. For most materials, when v_{cr} approaches a critical value v_L, G_f infinitely increases, and finally, the crack stops further accelerating (Ravi-Chandar and Knauss 1984; Dally et al. 1985; Fineberg et al. 1991; Shioya and Zhou 1995; Sharon et al. 1996).

Several approaches have been so far applied to examine dynamic fracturing. Nishioka (1995) and Nishioka et al. (2001) introduced the dynamic J-integral into a moving finite element mesh that needs a re-meshing algorithm with a very fine mesh around the crack tip. Belytschko and Black (1999) and Moes et al. (1999) suggested an extended FEM (XFEM) solution with crack propagation through ordinary elements which gives a smooth crack path with minimal re-meshing effort. However, discontinuities must be considered in the shape functions to model broken elements. It makes the solution too effortful when cracks intersect.

In resent years, cohesive finite element methods (CFEM) which are based on the cohesive zone concept, invented by Dugdale (1960) and Barenblatt (1962), have been extensively used. In a cohesive element, crack separation is expressed by a cohesive law linking crack surface traction to its opening displacement. Xu and Needleman (1994, 1995, 1996) have applied an elastic-exponentially decaying cohesive law. Camacho and Ortiz (1996, 1997) proposed a rigid-linear model law in 2D space. Later on, Pandolfi et al. (1999, 2000) and Ruiz et al. (2000) carried that out in 3D analysis. Zhai et al. (2004) analyzed dynamic fracture in two-phase Al_2O_3/TiB_2 ceramic composite microstructures using a CFEM. The model integrates cohesive surfaces along all finite element boundaries as an intrinsic part of the material description. This approach obviates the need for any specific fracture criteria and assigns models with the capability of predicting fracture paths and fracture patterns. Karedla and Reddy (2007) applied high inertia zone theory to a cohesive finite

T. Kazerani (✉) · G. F. Zhao · J. Zhao
Laboratoire de Mécanique des Roches (LMR),
Ecole Polytechnique Fédérale de Lausanne (EPFL),
EPFL/ENAC/IIC/LMR, Station 18,
1015 Lausanne, Switzerland
e-mail: tohid.kazerani@epfl.ch

element model to examine crack branching in PMMA. However, crack propagation speed was not fully discussed.

In all the research mentioned above, the cohesive laws used are rate-independent, i.e., the traction mobilized within the crack is just a function of its separation and independent of its opening speed. Much attention has been paid recently to the rate-dependent cohesive models. Li and Bazant (1997a, b) proposed a visco-elastic rate-dependent law to analyze a stationary crack under dynamic loading in concrete that results in cohesive forces extremely exceeding the material ultimate strength. Lee and Prakash (1999) studied dynamic fracturing in high-strength brittle steels. They found that the rate-dependency assumption was crucial to reproduce the experimental results. Zhou et al. (2005) introduced a linear decaying law into the cohesive interface elements to reproduce the laboratory results of PMMA cracking. They emphasized the necessity of considering rate-dependency to restrict the crack velocity. However, numerically predicted v_{cr} was still larger than v_L. Block et al. (2007) proposed the cohesive nodal force method, in which they assigned a continuum damage model to the solid elements, to control the model energy dissipation at high values of the loading rate.

In all the rate-dependent models reviewed, only the crack cohesive displacement (i.e., separation) is changing with the crack opening rate, and the crack cohesive strength is held fixed. This is contrary to most experimental observations which confirm that both the cohesive stress and displacement increase with the opening velocity (Li and Bazant 1997a, b; Costanzo and Walton 1998; Allen and Searcy 2001; Kubair et al. 2003; Xu et al. 2003; Ivankovic et al. 2004).

The aim of this study is to develop a "full" rate-dependent law in which both the cohesive stress and the displacement of the contact depend on its opening rate (Kazerani and Zhao 2010). This model is to be introduced into the distinct lattice spring method (DLSM) (Zhao et al. 2010a; Zhao and Zhao 2009) for simulating dynamic fracturing of the brittle materials. In coming sections, the experimental work done by Shioya and Zhou (1995) on dynamic crack propagation in PMMA plates is briefly reviewed. Following this, the DLSM methodology and the proposed rate-dependent cohesive law are explained in detail. Finally, the developed numerical model is used to reproduce the laboratory data. The simulation results show that our model is capable of reproducing the actual fracture energy and crack propagation velocity observed in the experiments.

2 Dynamic Crack Propagation in PMMA Plates

In this section, the experimental work done by Shioya and Zhou (1995) on fracturing behavior of pre-strained PMMA

strips is presented. More explanation in terms of the test setup and the experimental results is published by Zhou et al. (2005), and a detailed description is presented by Zhou (1996).

2.1 Experimental Setup and Measurement

Polymethyl methacrylate (PMMA) rectangular plate (3 mm thick) was used as the test material. Before crack propagation, a universal test machine loads the specimen in tension. The magnitude of the loading is measured by the load cell in the test machine. After reaching a given load level, a small sharp crack is initiated at the middle point of one specimen end by a razor. Because the material is very brittle, the small crack propagates straight across the specimen.

To record the crack propagation during the test, electric conductive lines are drawn on the specimen surface. They are connected to an electronic logic circuit. The output signal is recorded by a digital memory. The time when the crack cuts each line position is recorded in the digital memory. From this record, and the position of each line, the propagation history of the crack and its speed is obtained.

The data show that the crack velocity tends to a steady asymptotic value, and this steady propagation state continues even when the crack tip reaches the opposite edge of the specimen. The average steady velocity of the crack is called crack velocity and denoted by v_{cr}.

2.2 Test Results

Various specimens with different geometries are tested. The specimens are loaded to different levels of preloading before initiating the crack. By changing the tensile loading and the specimen shape, different values of elastic strain energy, W, are obtained. As the prescribed displacement is small compared to the specimen size, we consider the kinetic energy of the material in the region behind the crack front to be negligible. Therefore, the strain energy stored per unit length of the specimen is approximately equal to the energy consumed by the unit length of the crack propagation, i.e., the dynamic fracture toughness G_f. This equality is verified by Zhou et al. (2005) in detail.

From each test, a data point of (v_{cr}, G_f) is obtained. As shown in Fig. 1, these points are fitted with a monotonically-increasing curve which can be expressed by an empirical equation as follows:

$$G_f = G_0 \frac{v_L}{v_L - v_{cr}} \tag{1}$$

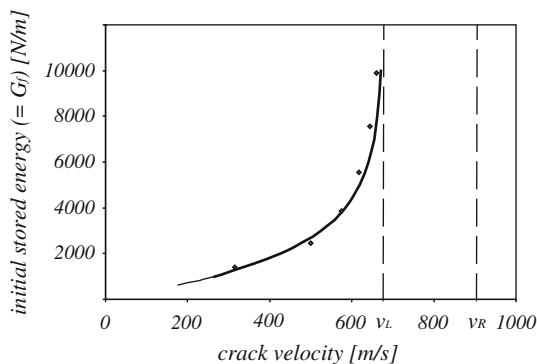where $v_L = 675$ m/s and $G_0 = 1,000$ N/m.

Fig. 1 The initial stored energy (i.e., fracture energy) versus the crack propagation velocity observed in the PMMA plates

3 The Distinct Lattice Spring Method (DLSM)

The DLSM (Zhao et al. 2010a; Zhao and Zhao 2009) is a microstructure-based numerical model based on the realistic multidimensional inter bond (RMIB) model (Zhao et al. 2010b). The RMIB model is an extension of the virtual multidimensional inter bond (VMIB) model (Zhang and Ge 2005) in which materials are discretized into mass particles (see Fig. 2). Whenever two particles are detected in contact, they are linked together through bonds between their center points. The multi-dimensional internal bond is adopted which includes one normal bond and one shear bond for both 2D and 3D. Due to the explicit consideration of the material microstructure, the proposed micromechanical model has the potential to give a more realistic approximation of the material failure behavior than a phenomenological model. Based on Cauchy-born rules and hyper-elastic theory, the relationship between the micromechanical parameters and the macro material constants, i.e., the Young's modulus and the Poisson ratio, can be obtained as follows (Zhang and Ge 2005):

$$k_n = \frac{3E}{\alpha^{3D}(1-2v)} \quad \text{and} \quad k_s = \frac{3(1-4v)E}{\alpha^{3D}(1+v)(1-2v)} \quad (2)$$

where k_n and k_s are the normal and shear stiffness of the inter-particle bond, respectively. E is the material Young's modulus, v the Poisson ratio and α^{3D} is the microstructure geometry coefficient which is obtained from

$$\alpha^{3D} = \frac{\sum l_i^2}{V} \quad (3)$$

where l_i denotes the initial length (before loading) of the bonds, and V is the volume of the model.

The particles and springs represent the material. The equation of motion of the system of particles and springs is expressed as
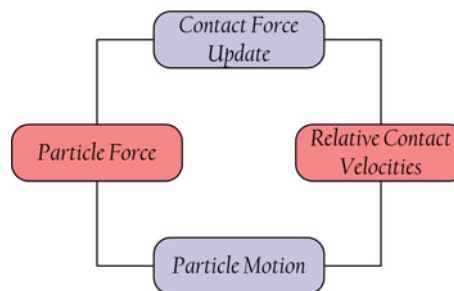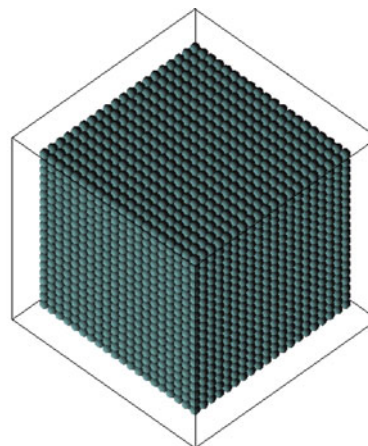

Fig. 2 The physical model (top) and the calculation cycle (bottom) of the DLSM

$$[\mathbf{K}]\mathbf{u} + [\mathbf{C}]\dot{\mathbf{u}} + [\mathbf{M}]\ddot{\mathbf{u}} = \mathbf{F(t)} \quad (4)$$

where $\mathbf{u}$ represents the particle displacement vector, $[\mathbf{M}]$ the diagonal mass matrix, $[\mathbf{C}]$ the damping matrix, and $\mathbf{F}(t)$ the vector of all external forces acting on the particles.

In the DLSM, the motion equations of the particle system are solved through the explicit central finite difference scheme. The calculation cycle is illustrated in Fig. 2. Given the particle displacements (either prescribed initially or obtained from the previous time step), new contacts and broken bonds are detected. The list of neighboring particles for each particle is updated. Then the contact and spring forces between the particles are calculated according to the prescribed force–displacement relations. The interaction between the particles is represented by one normal spring and one shear spring. The shear spring is a multi body spring which is different from the conventional lattice spring methods. Multi body means that the shear displacement is calculated from the local strain state which is determined from the displacement of a cloud of particles. Multi body spring is necessary to keep the rotational invariance and to allow the model to handle problems where the Poisson's ratio is larger than 0.25. The details are presented by Zhao et al. (2010a) and Zhao (2010). The behavior of the normal spring is in the conventional way,

which means that the normal deformation is directly calculated from the displacement of the two linked particles. For example, assume that there exists one bond between particles i and j, and the unit normal $\mathbf{n}(n_x, n_y, n_z)$ points form particle i to particle j. The relative displacement vector is calculated as

$$\mathbf{u}_{ij} = \mathbf{u}_j - \mathbf{u}_i \tag{5}$$

Then normal displacement vector and interaction force between two particles is given as

$$\mathbf{u}_{ij}^{\mathrm{n}} = (\mathbf{u}_{ij} \cdot \mathbf{n})\mathbf{n} \quad \text{and} \quad \mathbf{F}_{ij}^{\mathrm{n}} = k_n \mathbf{u}_{ij}^{\mathrm{n}} \tag{6}$$

where k_{n} is the normal spring stiffness and $\mathbf{n}$ is the normal to the bonds. The multi-body shear spring between two particles is introduced through a multi-body shear displacement vector:

$$\mathbf{u}_{ij}^{\mathrm{s}} = [\varepsilon]_{\mathrm{bond}}\mathbf{n}^{\mathrm{T}} - \left(([\varepsilon]_{\mathrm{bond}}\mathbf{n}^{\mathrm{T}}) \cdot \mathbf{n}\right)\mathbf{n} \tag{7}$$

where $[\varepsilon]_{\mathrm{bond}}$ is the bond strain state which is evaluated by the DLSM (Zhao et al. 2010a). Then the shear interaction between two particles is given as

$$\mathbf{F}_{ij}^{\mathrm{s}} = k_{\mathrm{s}}\mathbf{u}_{ij}^{\mathrm{s}} \tag{8}$$

where k_{s} is the stiffness of the shear spring. Equations 6–8 provide the force update for the DLSM. For displacement update, the particle velocity is calculated as

$$\dot{\mathbf{u}}_i^{(t+\Delta t/2)} = \dot{\mathbf{u}}_i^{(t-\Delta t/2)} + \frac{\sum \mathbf{F}_j^{(t)}}{m_p}\Delta t \tag{9}$$

where $\dot{\mathbf{u}}_i^{(t+\Delta t/2)}$ is the particle velocity at $t + \Delta t/2$, $\dot{\mathbf{u}}_i^{(t-\Delta t/2)}$ the particle velocity at $t - \Delta t/2$, m_p the particle mass, $\sum \mathbf{F}_j^{(t)}$ the sum of all the forces acting on the particle i including external forces, and δt the time step. Finally, the updated displacement of the particle is obtained as

$$\mathbf{u}_i^{(t+\Delta t)} = \mathbf{u}_i^{(t)} + \dot{\mathbf{u}}_i^{(t+\Delta t/2)}\Delta t \tag{10}$$

where $\mathbf{u}_i^{(t+\Delta t)}$ and $\mathbf{u}_i^{(t)}$ are the displacements at $t + \Delta t$ and t, respectively. Equations 9 and 10 form the main procedure involved in the DLSM.

3.1 Cohesive Law Used in the DLSM

The constitutive law implemented in the DLSM is shown in Fig. 3, where u represents the norm of $\mathbf{u}$, and u^* is its ultimate value beyond which the bond fails. δ_1 is the ratio of bond deformation to its ultimate deformation at the hardening point, and δ_2 is the same ratio but corresponding to the softening point (see Fig. 3).

There are three phases involved for each single bond: linear, hardening, and softening phase. The bond constitutive law is written as follows:

$$f = \begin{cases} k_{\mathrm{n}}u & \text{for} \quad u \leq \delta_1 u^* \\ k_{\mathrm{n}}u^*\delta_1 + \dfrac{(k_{\mathrm{red}}u^*\delta_2 - k_{\mathrm{n}}u^*\delta_1)(u - u^*\delta_1)}{u^*\delta_2 - u^*\delta_1} & \text{for} \quad \delta_1 u^* < u \leq \delta_2 u^* \\ k_{\mathrm{red}}u^*\delta_2 \dfrac{u^* - u}{u^* - u^*\delta_2} & \text{for} \quad \delta_2 u^* < u \leq u^* \end{cases} \tag{11}$$

k_{red} is called the initial softening stiffness and is defined in Fig. 3. The fracture energy, needed to fully open a unit area of a cracked surface in the DLSM model, is

$$G_{\mathrm{f}} = \frac{1}{2}\alpha E\left(\frac{u^*}{l^*}\right)^2 l^* \tag{12}$$

where l^* is the mean bond length in the whole DLSM model (Zhao 2010), and the dimensionless coefficient α is obtained by

$$\alpha = \delta_1^2 + (\delta_2 - \delta_1)\left(\delta_1 + \frac{k_{\mathrm{red}}}{k_{\mathrm{n}}}\delta_2\right) + \frac{k_{\mathrm{red}}}{k_{\mathrm{n}}}(1 - \delta_2)\delta_2 \tag{13}$$

Finally, the initial softening stiffness k_{red} is calculated in terms of the material tensile strength σ_{max} as

$$k_{\mathrm{red}} = k_{\mathrm{n}}\frac{1}{\delta_2}\frac{\sigma_{\mathrm{max}}}{E}\frac{l^*}{u^*} \tag{14}$$

Using Eqs. 12–14, k_{red} and u^* are calculated provided; we have δ_1 and δ_2. Because the obtained k_{red} and u^* are computed from the material properties (i.e., E, σ_{max}, G_{f}, etc.), which are evaluated from static fracturing, we call them rate-independent parameters. The parameters δ_1 and δ_2 are estimated by a simple trail and error, as explained later.

3.2 Rate-Dependent Model

To introduce rate effects into the DLSM, the initial softening stiffness and the ultimate bond deformation is assumed to change instantaneously with the bond deformation rate $\dot{u}$ as follows:
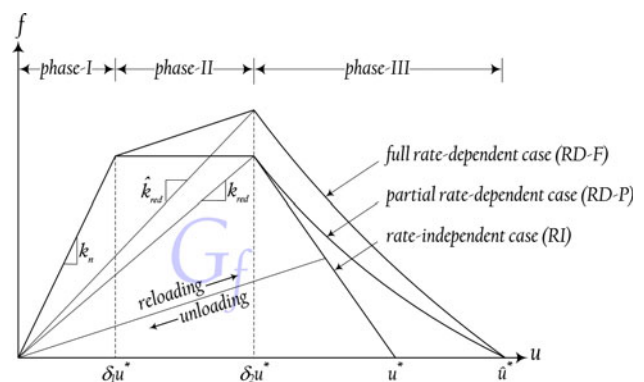

Fig. 3 The constitutive law used in the DLSM

$$\hat{k}_{\text{red}} = k_{\text{red}}\left(1 + \left(\frac{\dot{u}}{\dot{u}_{\text{ref}}^{k}}\right)^{\xi}\right) \text{ and } \hat{u}^* = u^*\left(1 + \left(\frac{\dot{u}}{\dot{u}_{\text{ref}}^{u}}\right)^{\eta}\right)$$

$$(15)$$

In Eq. 15, $\hat{k}_{\text{red}}$ and $\hat{u}^*$ are the rate-dependent values for the initial softening stiffness and the bond ultimate deformation. $\dot{u}_{\text{ref}}^{k}, \dot{u}_{\text{ref}}^{u}, \xi$, and η are model parameters which are adjusted such that the experimental results are reproduced. Their effect on the model response is discussed in Sect. 6. The validity of Eq. 15 is examined by Kazerani and Zhao (2010) in detail.

Expansion of Eq. 11 leads to Eq. 16, into which substituting $\hat{k}_{\text{red}}$ and $\hat{u}^*$ for k_{red} and u^* gives the rate-dependent cohesive law:

$$f = \begin{cases} k_{\text{n}}u & \text{for} \quad u \le \delta_1 u^* \\ k_{\text{n}}u^*\delta_1 + \dfrac{(\hat{k}_{\text{red}}u^*\delta_2 - k_{\text{n}}u^*\delta_1)(u - u^*\delta_1)}{u^*\delta_2 - u^*\delta_1} & \text{for} \quad \delta_1 u^* < u \le \delta_2 u^* \\ \hat{k}_{\text{red}}u^*\delta_2 \dfrac{\hat{u}^* - u}{\hat{u}^* - u^*\delta_2} & \text{for} \quad \delta_2 u^* < u \le \hat{u}^* \end{cases}$$

$$(16)$$

4 Modeling

To verify the model validity and adequacy, the laboratory tests introduced in Sect. 2 are simulated. The model geometry and mechanical properties are assumed the same as those used in the laboratory.

4.1 Material Properties

The PMMA material parameters are: density $\rho = 1{,}180$ kg/m^3, Young's modulus $E = 3{,}090$ MPa, Poisson ratio $v = 0.35$, tensile strength $\sigma_{\text{ten}} = 75$ MPa, and fracture energy $G_{\text{f}} = 300$ N/m. According to the elastic wave theory (Bedford and Drumheller 1996), longitudinal, shear, and Rayleigh surface wave speed are obtained as $c_{\text{L}} = 1{,}618$ m/s, $c_{\text{S}} = 985$ m/s, and $c_{\text{R}} = 906$ m/s, respectively. Note that the experimentally obtained limiting velocity of crack propagation, v_{L}, is about 70% of c_{R}.

4.2 Model Micro-Parameters and Geometry

The DLSM model is fully three-dimensional. The PMMA plate modeled is $l = 32$ mm, $h = 16$ mm, and contains a 4-mm-long edge crack along the centerline (see Fig. 4).

The plate is made of 512,000 particles with diameter of 0.1 mm. As seen in Fig. 2, all the particles have the same size and they are regularly packed. Therefore, the entire bonds have the same length, which is equal to the particle size, i.e., $l^* = 0.1$ mm in Eq. 12.

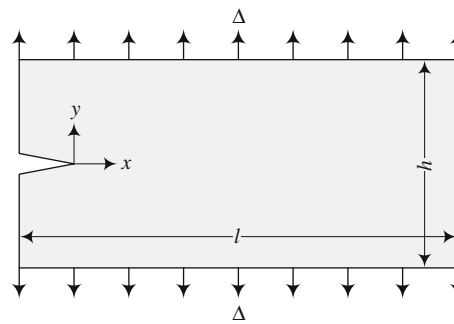**Fig. 4** The model geometry and boundary condition

Regarding Eq. 2, bond stiffness in tension and shear is calculated as $k_{\text{n}} = 219.67$ MN/m and $k_{\text{s}} = -65.09$ MN/m. In the rate-independent cohesive law (i.e., static fracturing), the bond strength σ_{max} and the ultimate bond deformation u^* are constant. $\sigma_{\text{max}} = 75$ MPa, which is assumed equal to the PMMA tensile strength.

As seen in Fig. 3, parameters $\delta_1 = 0.358$ is adjusted such that the maximum bond deformation at the end of phase-I becomes $\sigma_{\text{max}}/k_{\text{n}}$. Parameter $\delta_2 = 0.536$ is determined by a trail and error process explained in Sect. 6. Using Eqs. 12–14, the ultimate bond deformation $u^* = 6.78$ µm and $\alpha = 0.667$ are calculated to fit the given material fracture energy $G_{\text{f}} = 300$ N/m.

4.3 Boundary Conditions and Fracture Numerical Mechanism

As Fig. 4 illustrates, the plate is initially loaded by a prescribed tensile displacement Δ along the upper and lower boundaries in the y-direction, while the crack is not allowed to propagate yet. The specimen is not constrained in the x-direction. A static analysis is conducted to calculate the initial strain and stress states of the plate with the stationary crack. Under these loading circumstances, the strain energy W (per unit area) stored in the pre-strained plate is calculated by:

$$W = \frac{1}{2}\frac{E(2\Delta)^2}{h} = \frac{2E\Delta^2}{h}$$

$$(17)$$

After the static calculation, an explicit dynamic analysis is performed without changing the boundary conditions. The time step used in the dynamic solution should be shorter than the time of P-wave propagation through the lattice length as in classical explicit based methods, e.g., DEM and FEM. To satisfy that, the time step is taken as 0.01 µs which guarantees the numerical stability of the analysis.

Note that at end of the static stage, a high stress concentration is induced at the crack tip because of the pre-existing crack. This stress far exceeds the bond strength

and may lead to a sudden and extensive bond failure over the zone close to the crack tip during the first steps of the dynamic solution. However, after a short time, the crack will propagate in a steady state similar to what is observed in the laboratory (see Sect. 6).

As soon as a bond breaks during the steady crack propagation, the force distribution within the entire particle system will adapt itself with the model new geometry. It means that the tensile stress concentration moves toward the bonds, which are located at the new position of the crack tip. This tensile stress stretches the bonds and accelerates the particles. During this phase, the bond stiffness $\hat{k}_{red}$ and the ultimate displacement $\hat{u}^*$ are adjusted according to Eq. 15, and the bond force is continuously updated by Eq. 16. This procedure clearly shows how the crack propagates through the particle assemblage and the rate-dependent law controls the crack speed.

5 Crack Branching (Bifurcation)

The crack surface appearance varies when the crack velocity changes. The general tendency is that the surface roughness becomes larger when the crack velocity increases.

As described by Zhou et al. (2005), under low pre-strain ($\Delta < 0.10$ mm), the crack steady velocity is low ($v_{cr} < 450$ m/s), and the fractured surface is smooth. In moderate values of pre-strain ($\Delta = 0.10$–0.14 mm), the crack velocity is higher ($v_{cr} = 450$–600 m/s), and some streaks and roughness are observed on the crack surface. At first, these streaks are not remarkable. However, when the crack velocity approaches 600 m/s, they become deeper (0.01 mm order), but the crack still runs in a single straight path (Zhou et al. 2005; Fineberg 2006).

Under the highest pre-strain ($\Delta = 0.16$ mm), the crack velocity exceeds 600 m/s, and some small cracks start branching from the main crack. Generally, in the velocity range about 600–650 m/s, these small cracks stop further propagating and create the micro-branches seen in the laboratory. However, when $v_{cr} > 650$ m/s, one or few of these small cracks continue running as far as 1 mm or more, and crack bifurcation (branching) happens. A schematic representation of the crack bifurcation, observed by Zhou et al. (2005), is presented in Fig. 5.

A review on the fracture studies shows that the model mesh size cannot be lower than 0.1 mm order to have an efficient solution with the current computer facilities (Xu and Needleman 1994, 1995, 1996; Zhai et al. 2004; Zhou et al. 2005; Block et al. 2007; Kazerani and Zhao 2010; Zhao and Zhao 2009). The streaks and micro-branches,
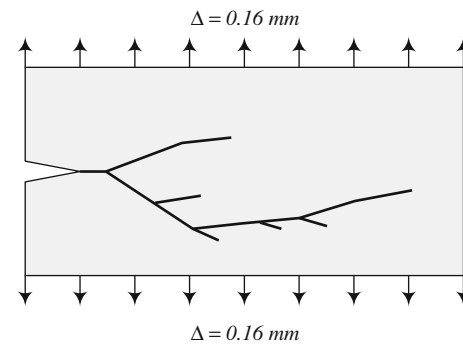

Fig. 5 A representative crack bifurcation observed in the highest pre-strain

observed on the crack surface, are much smaller than this value for low and moderate pre-strain. Therefore, crack branching could not be allowed in the numerical model except for the highest pre-strain where the branch size is larger than the mesh resolution.

6 Calculation Results and Discussion

The experimental results presented in Fig. 1 are compared with the predictions using the rate-independent (RI) and rate-dependent (RD) models.

In these models, crack propagation under six different loadings is determined. The prescribed boundary displacement Δ is chosen to be 0.06, 0.08, 0.10, 0.12, 0.14, and 0.16 mm. According to Eq. 17, the stored energy W is 1,391, 2,472, 3,863, 5,562, 7,571, and 9,888 N/m, respectively.

As shown in Fig. 3, the softening length in phase-III will decrease with increasing δ_2. However, we found that when δ_2 exceeds a threshold, equal to 0.536, the crack will arrest for the lowest pre-strain ($\Delta = 0.06$ mm) in the rate-independent model. For this reason, δ_2 can be finally determined from a trail and error process which finally led to $\delta_2 = 0.536$.

There are two rate-dependent (RD) cases possible:

- Partial rate-dependency, RD-P: Only u^* is rate-dependent, while k_{red} is held constant.
- Full rate-dependency, RD-F: Both k_{red} and u^* change in terms of the bond deformation rate.

Results using the RI case are presented in Fig. 6 in terms of the crack tip position versus Δ where the crack speed for each value of Δ is computed by the average slope of the corresponding curve. As seen, the crack propagates in a steady state, and no fluctuation or instability is observed in the crack speed response.
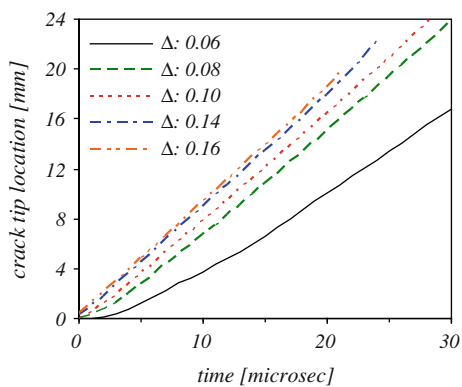
Fig. 6 The crack tip location versus time in the rate-independent (RI) case
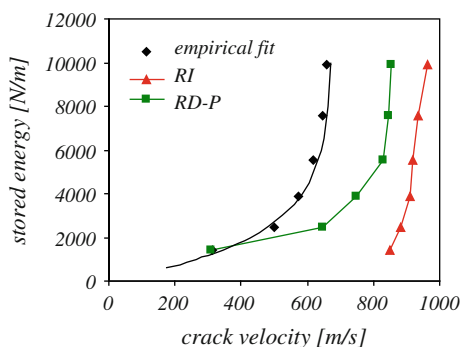

Fig. 7 The variation of the crack velocity versus the initial stored energy of the plate for the rate-independent (RI) and the partial rate-dependent (RD-P) model

6.1 Partial Rate-Dependent Case

The RD-P modeling logic is similar to the cohesive element model by Zhou et al. (2005) and the cohesive nodal force model of Block et al. (2007). In Fig. 7, the experimental results are compared with those of the RI and RD-P model, with $\dot{u}_{ref}^u = 16$ m/s and $\eta = 1.0$. As seen, the crack velocity in the RI model is about the Rayleigh wave speed, which is much higher than the limiting velocity v_L observed in the laboratory. This proves that the rate-independent models are not applicable to dynamic fracturing, and the rate effects have to be introduced into the model.

Although the RD-P model results in better predictions, it cannot precisely reproduce the laboratory results. As argued by Zhou et al. (2005), numerically obtained crack speed directly depends on the magnitude of the fracture energy G_f released at each bond failure. Since the bond strength is held constant in the RD-P model, G_f increase is limited to the increase in u^*. Hence, the fracture energy release cannot be adequately reproduced.

Zhou et al. (2005) claimed that the crack branching allowance solves this problem. Block et al. (2007) assigned a damage model to the solid material to increase the fracture energy and control the crack speed. These two methods artificially treat the discussed lack of energy dissipation through the bond failure. As described in Sect. 5, Zhou's solution (i.e., crack branching allowance) is not in agreement with the specimen post-fracture appearance in low and moderate pre-strain where no branching is observed in the plate. Application of a damage model for solid elements by Block et al. (2007) does not sound quite convincing, because the majority of the energy dissipation seems to happen within the damaged solid material, not in the cracked surface.

One may think that the RD-P model may lead to better results by changing η or $\dot{u}_{ref}^u$. However, as discussed by Zhou et al. (2005), this model never properly reproduces the laboratory results, and sometimes causes an unrealistically high bond deformation that even exceeds the prescribed boundary displacement (i.e., 2Δ).

6.2 Full Rate-Dependent Case

As observed in the laboratory, cracking in a fast moving crack-tip zone may result in local stress increase (Costanzo and Walton 1998; Allen and Searcy 2001; Kubair et al. 2003; Xu et al. 2003; Ivankovic et al. 2004). A quantitative evaluation, performed by Zhou and Molinari (2004), shows that the failure strength of ceramics increases up to 15% when the strain rate increases from 40 to 5,000 s^{-1}. This stress increase raises G_f and consequently influences on the material fracturing behavior.

All the previous discussions make us believe that each bond break must dissipate enough energy to limit the crack speed, and both the bond cohesive strength and deformation must be increased to produce the actual fracture energy. This idea led to the development of a full rate-dependent model (RD-F) in which both u^* and k_{red} change with $\dot{u}^*$.

A comparison of the laboratory results, RD-P and RD-F simulations, is shown in Fig. 8. The rate-dependency
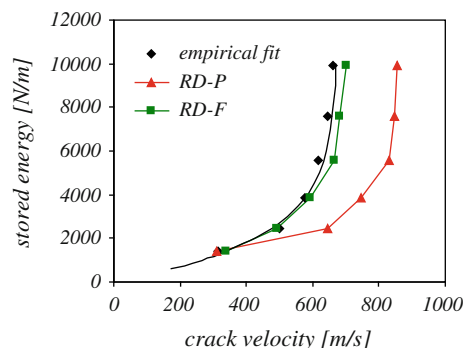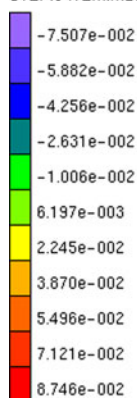

Fig. 8 Variation of the crack velocity versus the initial stored energy of the plate for the full rate-dependent (RD-F) model
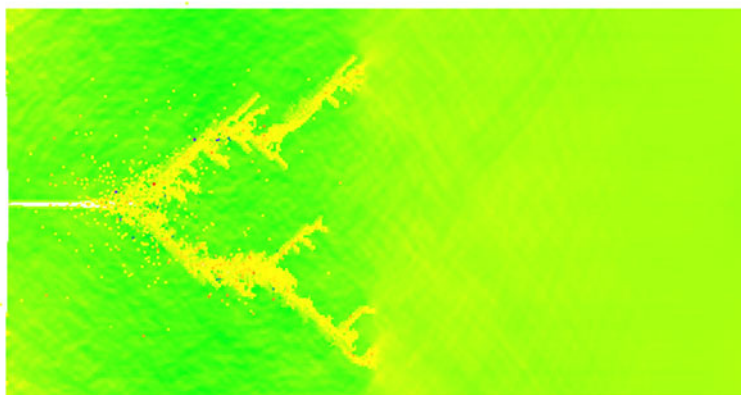
Fig. 9 Distribution of the
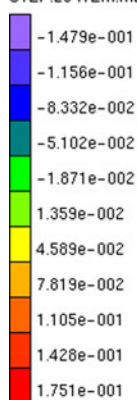y-direction strain, predicted by
the DLSM at $t = 5$ μs (**a**) and
$t = 25$ μs (**b**) for the highest
pre-strain

parameters are taken as $\dot{u}_{ref}^{u} = 40.0$ m/s, $\dot{u}_{ref}^{k} = 5.0$ m/s, $\eta = 4.0$, and $\xi = 0.2$ by trail and error to get the best fit. As seen in Fig. 8, while the RD-P solution approaches unrealistically high cracking speed for large values of stored energy, the RD-F follows the experimental data and closely predicts the PMMA fracture response.

According to the discussion in Sect. 5, no crack branching is permitted in the model for low and moderate pre-strain, and the crack propagates in a straight path only. However, in the highest value of prescribed loading ($\Delta = 0.16$ mm), the crack is allowed to bifurcate. The results of branching for this case are presented in Fig. 9. It shows that the numerically obtained branching pattern is quite similar to the laboratory results observed by Shioya and Zhou (1995) and Zhou et al. (2005) (see Fig. 5).

7 Conclusions

Dynamic fracture behavior of PMMA, a brittle material, was explored using a rate-dependent model implemented in the DLSM. The proposed model increases both the ultimate deformation and the strength of the bonds in terms of their deformation rate.

Since the magnitude of the micro-branches, experimentally observed on the cracked surface for low and moderate pre-strain, is much smaller than the finest possible mesh size, no crack branching was allowed, and the model assumes the crack to propagate through a straight path within the plate. However, as the crack branch size in high pre-strain is comparable with the model mesh resolution, the crack bifurcation was allowed in this situation.

The model reproduces the actual energy dissipation through the cracked surface. It also predicts the laboratory crack velocity for all values of the prescribed loading, as well as the branching pattern observed in high pre-strain. All these achievements are reached while no additional assumptions, like introducing a damage model (Block et al. 2007) or unnecessary branching (Zhou et al. 2005), are required.

The obtained results verify the validity and the adequacy of the proposed model to effectively predict the fracture behavior of the brittle materials.

References

Allen DH, Searcy CR (2001) Micromechanically-based model for predicting dynamic damage evolution in ductile polymers. Mech Mater 33(3):177–184

Barenblatt GI (1962) The mathematical theory of equilibrium cracks in brittle fracture. Adv Appl Mech 7:55–129

Bedford A, Drumheller DS (1996) Introduction to elastic wave propagation. Wiley, New York

Belytschko T, Black T (1999) Elastic crack growth in finite elements with minimal re-meshing. Int J Numer Methods Eng 45(5):601–620

Block G, Rubin M et al (2007) Simulations of dynamic crack propagation in brittle materials using nodal cohesive forces and continuum damage mechanics in the distinct element code LDEC. Int J Fract 144(3):131–147

Broberg KB (1999) Cracks and fracture. Academic Press, New York

Camacho GT, Ortiz M (1996) Computational modeling of impact damage in brittle materials. Int J Solids Struct 33(20–22):2899–2938

Camacho GT, Ortiz M (1997) Adaptive Lagrangian modeling of ballistic penetration of metallic targets. Comput Methods Appl Mech Eng 142(3–4):269–301

Costanzo F, Walton JR (1998) Numerical simulations of a dynamically propagating crack with a nonlinear cohesive zone. Int J Fract 91(4):373–389

Dally JW, Fourney WL et al (1985) On the uniqueness of the stress intensity factor—crack velocity relationship. Int J Fract 27(3–4):159–168

Dugdale DS (1960) Yielding of steel sheets containing slits. J Mech Phys Solids 8(2):100–104

Fineberg J (2006) The dynamic of rapidly moving tensile cracks in brittle amorphous material. In: Arun S (ed) Dynamic fracture mechanics. World Scientific, Singapore, pp 104–146

Fineberg J, Gross SP et al (1991) Instability in dynamic fracture. Phys Rev Lett 67(4):457–460

Freund LB (1990) Dynamic fracture mechanics. Cambridge University Press, Cambridge

Ivankovic A, Pandya KC et al (2004) Crack growth predictions in polyethylene using measured traction-separation curves. Eng Fract Mech 71(4–6):657–668

Karedla RS, Reddy JN (2007) Modeling of crack tip high inertia zone in dynamic brittle fracture. Eng Fract Mech 74(13):2084–2098

Kazerani T, Zhao J (2010) Simulation of dynamic fracturing in brittle materials using discrete element method and a full rate-dependent logic for cohesive contact. Eng Fract Mech (submitted)

Kubair DV, Geubelle PH et al (2003) Analysis of a rate-dependent cohesive model for dynamic crack propagation. Eng Fract Mech 70(5):685–704

Lee Y, Prakash V (1999) Dynamic brittle fracture of high strength structural steels under conditions of plane strain. Int J Solids Struct 36(22):3293–3337

Li YN, Bazant ZP (1997a) Cohesive crack with rate-dependent opening and visco-elasticity: I. Mathematical model and scaling. Int J Fract 86(3):247–265

Li YN, Bazant ZP (1997b) Cohesive crack model with rate-dependent opening and visco-elasticity: II. Numerical algorithm, behavior and size effect. Int J Fract 86(3):267–288

Moes N, Dolbow J et al (1999) A finite element method for crack growth without re-meshing. Int J Numer Methods Eng 46(1):131–150

Nishioka T (1995) Recent developments in computational dynamic fracture mechanics. In: Aliabadi MH (ed) Dynamic fracture mechanics, chap 1. Computational Mechanics Publications, Southampton, pp 1–60

Nishioka T, Tokudome H et al (2001) Dynamic fracture-path prediction in impact fracture phenomena using moving finite element method based on Delaunay automatic mesh generation. Int J Solids Struct 38(30–31):5273–5301

Pandolfi A, Krysl P et al (1999) Finite element simulation of ring expansion and fragmentation: the capturing of length and time scales through cohesive models of fracture. Int J Fract 95(1–4):279–297

Pandolfi A, Guduru PR et al (2000) Three dimensional cohesive-element analysis and experiments of dynamic fracture in C300 steel. Int J Solids Struct 37(27):3733–3760

Ravi-Chandar K, Knauss WG (1984) An experimental investigation into dynamic fracture: II. Microstructural aspects. Int J Fract 26(1):65–80

Ruiz G, Ortiz M et al (2000) Three-dimensional finite-element simulation of the dynamic Brazilian tests on concrete cylinders. Int J Numer Methods Eng 48(7):963–994

Sharon E, Gross SP et al (1996) Energy dissipation in dynamic fracture. Phys Rev Lett 76(12):2117–2120

Shioya T, Zhou F (1995). Dynamic fracture toughness and crack propagation in brittle material. In: Constitutive relation in high/very high strain rates, pp 105–112

Xu XP, Needleman A (1994) Numerical simulations of fast crack growth in brittle solids. J Mech Phys Solids 42(9):1397–1434

Xu XP, Needleman A (1995) Numerical simulations of dynamic interfacial crack growth allowing for crack growth away from the bond line. Int J Fract 74(3):253–275

Xu XP, Needleman A (1996) Numerical simulations of dynamic crack growth along an interface. Int J Fract 74(4):289–324

Xu C, Siegmund T et al (2003) Rate-dependent crack growth in adhesives: I. Modeling approach. Int J Adhes Adhes 23(1):9–13

Zhai J, Tomar V et al (2004) Micromechanical simulation of dynamic fracture using the cohesive finite element method. J Eng Mater Technol 126(2):179–191

Zhang ZN, Ge XR (2005) Micromechanical consideration of tensile crack behavior based on virtual internal bond in contrast to cohesive stress. Theor Appl Fract Mech 43:342–359

Zhao GF (2010) Development of micro-macro continuum-discontinuum coupled numerical method, PhD thesis. EPFL

Zhao GF, Zhao J (2009) Microscopic numerical modeling of the dynamic strength of brittle rock. In: Proceedings of ICADD9

analysis of discontinuous deformation: new developments and applications, pp 633–640

Zhao GF, Fang J, Zhao J (2010a) A 3D distinct lattice spring method for elasticity and dynamic failure. Int J Numer Anal Methods Geomech (submitted)

Zhao GF, Fang J, Zhao J (2010b). A new microstructure-based constitutive model for failure modeling of elastic continuum. Eur J Mech Solid (submitted)

Zhou F (1996) Study on the macroscopic behavior and the microscopic process of dynamic crack propagation, PhD dissertation. The University of Tokyo, Tokyo

Zhou F, Molinari JF (2004) Stochastic fracture of ceramics under dynamic tensile loading. Int J Solids Struct 41(22–23):6573–6596

Zhou F, Molinari J-F et al (2005) A rate-dependent cohesive model for simulating dynamic crack propagation in brittle materials. Eng Fract Mech 72(9):1383–1410